3-D Flight Performance Simulation of a Liquid-Filled Quadrotor

Article *in* International Journal of Aeronautical and Space Sciences · April 2025

DOI: 10.1007/s42405-025-00923-9

7 authors, including:

Jipeng Li
Soochow University
30 PUBLICATIONS **569** CITATIONS
SEE PROFILE

D.Q. Cao
Harbin Institute of Technology
265 PUBLICATIONS **4,959** CITATIONS
SEE PROFILE

Xianglong Su
Soochow University
20 PUBLICATIONS **258** CITATIONS
SEE PROFILE

Jae-Hung Han
Korea Advanced Institute of Science and Technology
385 PUBLICATIONS **6,115** CITATIONS
SEE PROFILE

International Journal of Aeronautical and Space Sciences
https://doi.org/10.1007/s42405-025-00923-9

IJASS International Journal of Aeronautical and Space Sciences

ORIGINAL PAPER

3-D Flight Performance Simulation of a Liquid-Filled Quadrotor

Jipeng Li[1,2,3] · Ming Cao[1] · Fan Wang[1] · Dengqing Cao[3,4] · Yishen Tian[5] · Xianglong Su[1] · Jae-Hung Han[2]

Received: 3 October 2024 / Revised: 16 February 2025 / Accepted: 17 February 2025

Abstract
The modeling of a quadrotor with complex internal or external loads is rather important and difficult in terms of ensuring accurate trajectory tracking and strong robustness. This paper mainly studies the dynamics performance of a liquid-filled quadrotor in a 3-D maneuvering flight environment. The non-inertial smoothed particle hydrodynamics (NI-SPH) method is adopted for the precise modeling of the liquid. Derivations for the rigid dynamics model of the quadrotor based on Newton–Euler formulation are also conducted. A multi-scale time stepping iteration method is introduced here for the fluid–structure interaction (FSI) iteration framework. This work enforces the quadrotor's 3-D commanded trajectory and simulates the dynamics performance of the coupled system. Three different types of loads, empty load, constant load, and sloshing load, are systematically compared. Results show that the quadrotor with a sloshing load usually has a higher overshoot compared with the other two cases. The trajectory tracking error in the vertical direction is much smaller than those in horizontal directions. Moreover, the quadrotor with an onboard load damped much faster when it stops to hover, which is because of the gravity angular stiffness. Sloshing effect deteriorates the position and attitude tracking accuracy, which leads to the fluctuation in the speeds of the UAV rotors. The sloshing forces in horizontal and vertical directions are around 20% and 5% of the weight of the whole liquid. These results help to gain a better understanding of the sloshing behaviors and could enlighten researches on slosh suppression methods in future.

Keywords Fluid–structure interaction · Liquid-filled quadrotor · Attitude-liquid-control coupling dynamics · Liquid sloshing · Non-inertial SPH

1 Introduction

Unmanned aerial vehicles (UAVs), commonly known as drones, were originally developed for dull, dirty or dangerous missions. Due to recent advances in control technologies and reduced manufacturing costs, their use has expanded to many applications such as plant protection, product deliveries, aerial photography, policing and surveillance, infrastructure inspections, and other scientific uses. Different UAVs of the same type generally have similar components. The main exceptions, however, are the payloads, which depend on the missions or the operational environments of UAVs. For example, tactical UAVs installed with reconnaissance cameras could bring photos back, agriculture drones with pesticide on board prevent exposure of workers to toxic chemicals.

The fluid/structure interaction (FSI) between the UAV and environment is a classic problem. For the complexity and stochastic of flow, the FSI can be hard to simulated and predicted. Sometimes the FSI is treated as an uncertain disturbance, which is also a key scientific problem during engineering analysis. The FSI could also be classified

Communicated by Seungkeun Kim.

✉ Xianglong Su
xlsu@suda.edu.cn

✉ Jae-Hung Han
jaehunghan@kaist.ac.kr

1 School of Rail Transportation, Soochow University, Suzhou 215131, People's Republic of China

2 Department of Aerospace Engineering, Korea Advanced Institute of Science and Technology, 291 Daehak-Ro, Yuseong-Gu, Daejeon 34141, Republic of Korea

3 School of Astronautics, Harbin Institute of Technology, Harbin 150001, People's Republic of China

4 Center for Dynamics and Intelligent Control Research, School of Mathematics and Statistics, Shandong University of Technology, Zibo 255000, People's Republic of China

5 Zhiyuan Research Institute, Hangzhou 310012, People's Republic of China

Published online: 02 April 2025

into two specific problems, the wind disturbance and the sloshing disturbance. The complex wind filed, for example, has a significant impact on the flight performance of UAV [1]. To realize anti-disturbance operation, Kim [2] reviewed the flight control law technologies for flying qualities. Hassani [3] and Bui [4] proposed model-based control law and Lyapunov-based control law for attitude trajectory tracking of UAV. These work enlighten us that to study the FSI problem of the UAV, we have only two ways. One is the researches on fluid mechanics for an in-depth understanding of the flow field. The other one is the robust control system of the UAV which could guarantee the fault-tolerance under disturbances. As for the sloshing disturbance problems, Gerrits and Veldman [5] studied the dynamics of liquid-filled spacecraft and proposed a method for simulating coupled liquid–solid dynamics of a satellite carrying fuel. Feng et al. [6] built a model of a micro UAV with a slung load and simulated it. Their results verified that the trajectory of the payload is complicated and periodically varying around the commanded trajectory. Further, a more realistic helicopter/slung-load system under the flexible sling hypothesis was recently proposed by Cao et al. [7]. They pointed out that the traditional rigid sling model is not precise enough, and the flexibility of the sling will worsen the dynamic stability and flight quality of the coupled system. Sayyaadi et al. [8] studied the cooperative transport of a liquid-filled tank using quadrotors. By modeling the liquid as an equivalent mass-spring system, they showed that both the slung load and sloshing effect impeded stabilization of the quadrotors by the controller. The above literature review shows that the simulation algorithm for UAVs under time-varying and uncertain loads still remains a challenge.

Liquid sloshing, an onboard load that is the focus of this paper, has similar characteristics with the slung load. Both of them are negligible for their considerable inertia and periodical impulses. However, it should be noted that the most important difference between them in a simulation is the modeling complexity. Due to the difficulties in modeling and computation cost, equivalent mechanical models, compared to CFD methods [9–14], are widely adopted. Ibrahim et al. [15] reviewed the progress in liquid sloshing dynamics and illustrated equivalent mechanical modeling methods for a rectangular container and a cylindrical tank. As for liquid-filled spacecraft, Yue [16] and Wang [17] proposed control strategies for sloshing suppression and attitude stabilization. Chung et al. [18] simulated the vibration of a SAR antenna reflector during maneuvering under the effect of propellant sloshing. Based on the pendulum equivalent model, a moving pulsating ball model was proposed [19], and some new parameter setting methods for the equivalent mechanical model such as particle swarm optimization, pendulum equation, and bouncing ball model have also recently been reported [20–25].

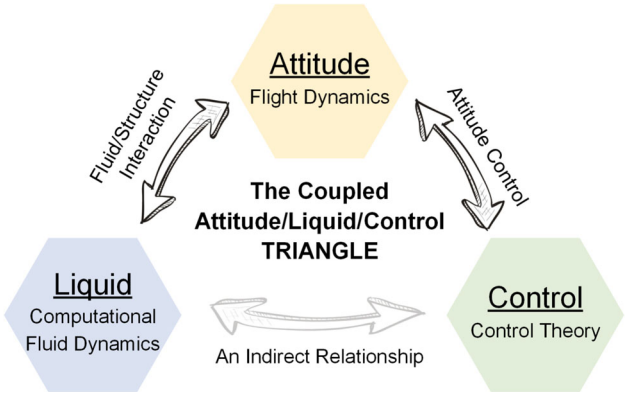

Fig. 1 The coupled attitude/liquid/control triangle

To further understand the logic between the UAV attitude, liquid sloshing, and flight control, a coupled triangle is shown in Fig. 1. Studies on attitude, liquid, and control require the theories of flight dynamics, CFD, and control, respectively. Interdisciplinary researches however, also motivates the development of new theory. FSI, for instance, is a coupled problem between UAV attitude and liquid sloshing. The attitude control is also an area of interdisciplinary research that spans rigid body dynamics and control theory. In fact, there is an indirect interaction between sloshing and control, and the UAV attitude is their link. To deal with the strong coupling and large-amplitude free-surface waves, the smoothed particle hydrodynamics (SPH) [26–30], a novel CFD method, has advantages. Based on the compressibility, the SPH method may be classified into two categories—incompressible SPH (ISPH) [31–33] and weakly compressible SPH (WCSPH) [34, 35]. These methods have respective advantages, and many comparisons have been reported [36, 37]. With ongoing development over the past several decades, many advanced algorithms have been proposed such as SPH based on the Riemann solver, δ^+-SPH, KCSPH, and so on [38–42]. Wang et al. [43] proposed a non-inertial SPH (NI-SPH) method for rapid simulation of 3D sloshing in a lunar soft-landing spacecraft. In their work, a non-inertial coordinate system was used to derive transient external excitations to liquid. The sloshing force and moment exerted by liquid against the spacecraft were then calculated by the linear and angular momentum theorems of the particle system, which circumvents the integration of pressures. The sloshing was well simulated in their work based on the practical stochastic excitations under a low-gravity environment. As mentioned before, the analysis of strongly coupled nonlinear large-amplitude free-surface waves is known to be very difficult. The authors reported their work on the vibration analysis of an SAR antenna reflector during satellite maneuvering considering the sloshing effect [18] and the framework of FSI by the ISPH method [44, 45], and the Riemann-SPH method [46]. The dynamics performance of a liquid-filled quadrotor under real-time control

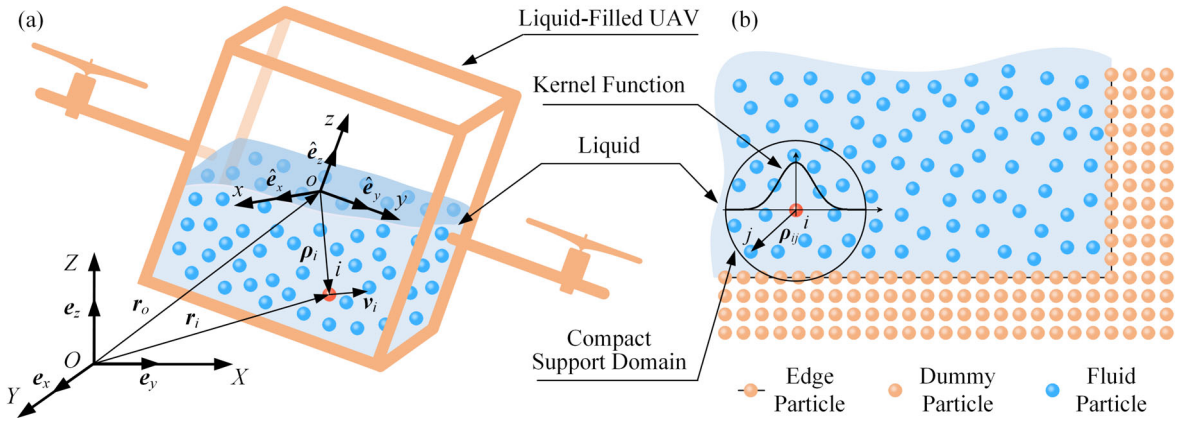

Fig. 2 Coordinate scheme of the liquid-filled UAV system and the non-inertial SPH method

was simulated and analyzed. The tracking trajectories in reference [45] is in-plane and spatial trajectory tracking problem is not mentioned.

This paper gives a further development of the dynamics performance simulation of a liquid-filled quadrotor in a 3-D maneuvering flight environment, and also provides an analysis of its trajectory tracking performance in some numerical cases. The contributions of this paper are as follows: (1) an algorithm for the attitude/liquid/control coupled model of a liquid-filled quadrotor in a 3-D maneuvering flight environment by the non-inertial SPH method is proposed; (2) the algorithm is realized and the dynamics performance simulation results are simulated; and (3) comparisons between empty load/constant-load/sloshing-load cases are conducted and the quantificational influences of the mass effect and the sloshing effect are analyzed and summarized.

The paper is organized as follows. Section 2 presents the derivation process of the non-inertial SPH method. Section 3 builds the dynamics model of the liquid-filled quadrotor, designs the controller, and introduces the iteration framework. Section 4 analyses the simulation performance of the quadrotor in a 3-D maneuvering environment and compares the system outputs under different kinds of loads. Section 5 summarizes the whole work and draws conclusions.

2 Non-Inertial ISPH Schemes

2.1 General Method of Free-Surface Waves by ISPH

The derivations of the ISPH method touch on the expressions of particle positions in different coordinates. Therefore, the scheme shown in Fig. 2 is provided for a better understanding of the derivations. Define $I = \{OXYZ\}$ denoting an earth-fixed inertial frame and $A = \{oxyz\}$ a body-fixed non-inertial frame whose origin o is at the center of geometry of the quadrotor.$(\mathbf{e}_x, \mathbf{e}_y, \mathbf{e}_z)^{\mathrm{T}}$ and $(\hat{\mathbf{e}}_x, \hat{\mathbf{e}}_y, \hat{\mathbf{e}}_z)^{\mathrm{T}}$ are the unit vectors of frames I and A. The absolute position and velocity of the origin o in the body frame are defined by $\mathbf{r}_o = (x, y, z)^{\mathrm{T}}$ and $\mathbf{v}_o = (v_x, v_y, v_z)^{\mathrm{T}}$, respectively. Three Euler angles and angular velocities are defined as $\boldsymbol{\Theta} = (\phi, \theta, \psi)^{\mathrm{T}}$ and $\boldsymbol{\Omega} = (p, q, r)^{\mathrm{T}}$. The position of particle i in frame A is $\boldsymbol{\rho}_i = x_i\hat{\mathbf{e}}_x + y_i\hat{\mathbf{e}}_y + z_i\hat{\mathbf{e}}_z$ and its position vector in frame I is $\mathbf{r}_i$.

Given the incompressibility, the Reynolds-Averaged Navier–Stokes equations in the Lagrangian frame, including the mass and momentum equations, are obtained by substituting the SPH approximations into these equations [28, 31], that is,

$$-\frac{1}{\rho_i}\sum\nolimits_j m_j \mathbf{v}_{ij}^r \cdot \nabla_i W_{ij} = 0, \tag{1a}$$

$$\frac{\mathrm{d}\mathbf{v}_i}{\mathrm{d}t} = -\sum\nolimits_j m_j\left(\frac{p_i}{\rho_i^2} + \frac{p_j}{\rho_j^2}\right)\nabla_i W_{ij} + \sum\nolimits_j \frac{4m_j(\mu_i + \mu_j)}{(\rho_i + \rho_j)^2} \times \frac{\mathbf{r}_{ij} \cdot \nabla_i W_{ij}}{|\mathbf{r}_{ij}|^2 + 0.01h^2} \cdot \mathbf{v}_{ij} + \mathbf{a}_{\mathrm{body}}, \tag{1b}$$

where $\mathbf{W}_{ij} = \mathbf{W}(\mathbf{r}_i - \mathbf{r}_j, h) = \mathbf{W}(\mathbf{r}_{ij}, h)$ is a kernel function with a finite support and h is the smooth length that is related to the radius of compact support region; the subscripts i and j denote particle i and particle j (particle j is in the support region of particle i);$\mathbf{r}_{ij} = \mathbf{r}_i - \mathbf{r}_j$ is the position vector between two particles in the inertial frame; $\mathbf{v}_{ij} = \mathbf{v}_i - \mathbf{v}_j$ and $\mathbf{v}_{ij}^r = \mathbf{v}_i^r - \mathbf{v}_j^r$ are the absolute velocities and relative velocities between two particles i and j in the inertial frame and non-inertial frame, respectively;m, ρ, p, μ are the mass, density, pressure, dynamics viscosity of the fluid particles, respectively; and $\mathbf{a}_{\mathrm{body}}$ is the body acceleration such as gravity acceleration or inertial acceleration, which will be described in detail in the next subsection.

A 5th-order quintic spline kernel function in three-dimensional space is adopted as follows [28, 44]

$$W(\mathbf{r}_{ij},\, h) = \frac{3}{359\pi h^3} \times \begin{cases} (3-R)^5 - 6(2-R)^5 + 15(1-R)^5,\ 0 \le R < 1 \\ (3-R)^5 - 6(2-R)^5,\ 1 \le R < 2 \\ (3-R)^5,\ 2 \le R < 3 \\ 0,\ R \ge 3 \end{cases}$$

where $R = |\mathbf{r}|/h$.

A two-step calculation method is introduced here to solve the equations above. It consists of a prediction step and a correction step. In the prediction step, the intermediate velocity of the particle is first derived by explicit integration with only viscous term and body acceleration term,

$$\frac{\mathbf{v}_i^{r,*} - \mathbf{v}_i^{r,n}}{\Delta t} = \sum\nolimits_j \frac{4m_j(\mu_i + \mu_j)}{(\rho_i + \rho_j)^2} \frac{\mathbf{r}_{ij} \cdot \nabla_i W_{ij}}{|\mathbf{r}_{ij}|^2 + 0.01h^2} \cdot \mathbf{v}_{ij} + \mathbf{a}_{\text{body}}, \tag{2}$$

where $\mathbf{v}_i^{r,*}$ is the intermediate velocity of particle i and $\mathbf{v}_i^{r,n}$ is the relative velocity of particle i at time n (present time). Δt is the numerical time step of the ISPH method.

In the correction step, the corrected velocity is obtained based on the pressure term only, that is [32]

$$\frac{\mathbf{v}_i^{r,n+1} - \mathbf{v}_i^{r,*}}{\Delta t} = -\frac{1}{\rho_i} \nabla p_i^{n+1}, \tag{3}$$

where $\mathbf{v}_i^{r,n+1}$ is the corrected relative velocity of particle i at time $n+1$ (next time step). Let the intermediate velocity be projected on the divergence-free space by rewriting Eq. (3); we can then obtain

$$\nabla \cdot \left(\frac{\mathbf{v}_i^{r,n+1} - \mathbf{v}_i^{r,*}}{\Delta t} \right) = -\nabla \cdot \left(\frac{1}{\rho_i} \nabla p_i^{n+1} \right). \tag{4}$$

In general, the intermediate velocity is not divergence-free [31, 32]. Therefore, the following pressure equation, with the consideration of incompressibility, can be derived:

$$\nabla^2 p_i^{n+1} = \frac{\rho_i}{\Delta t} \nabla \cdot \mathbf{v}_i^{r,*}. \tag{5}$$

By solving pressure from the pressure Poisson equation (PPE), Eq. (5), the velocity of particles can be updated by calculating the pressure gradient from Eq. (3):

$$\mathbf{v}_i^{r,n+1} = \mathbf{v}_i^{r,*} - \left(\frac{\Delta t}{\rho_i} \nabla p_i^{n+1} \right). \tag{6}$$

Then the positions of particles can be easily integrated by

$$\rho_i^{n+1} = \rho_i^n + \left(\frac{\mathbf{v}_i^{r,n+1} + \mathbf{v}_i^{r,*}}{2} \right) \Delta t. \tag{7}$$

Equations here give the SPH approximation forms of the terms shown in Eqs. (5–7):

$$\nabla^2 p_i = \frac{2}{\rho_i} \sum\nolimits_j m_j \frac{p_{ij}\mathbf{r}_{ij}}{|\mathbf{r}_{ij}|^2 + 0.01h^2} \cdot \nabla_i W_{ij}, \tag{8a}$$

$$\nabla \cdot \mathbf{v}_i^r = -\frac{1}{\rho_i} \sum\nolimits_j m_j \mathbf{v}_{ij}^r \nabla_i W_{ij}, \tag{8b}$$

$$\nabla p_i = \rho_i \sum\nolimits_j m_j \left(\frac{p_i}{\rho_i^2} + \frac{p_j}{\rho_j^2} \right) \nabla_i W_{ij}. \tag{8c}$$

2.2 Inertial Force of Particles Due to the Composite Motion

The last subsection introduces the ISPH for free-surface waves in the body-fixed frame without frame transformations (both translations and rotations). The influences of frame transformations is described here.

For a certain fluid particle i, its positions in the inertial frame and the non-inertial frame are $\mathbf{r}_i$ and $\boldsymbol{\rho}_i$, respectively. The transformation between $\mathbf{r}_i$ and $\boldsymbol{\rho}_i$ can be easily achieved by a translation and a rotation, given as $\mathbf{r}_i = \mathbf{r}_o + \mathbf{R}_s \boldsymbol{\rho}_i$, and

$$\mathbf{R}_s = \begin{pmatrix} \cos\theta\cos\psi & \sin\phi\sin\theta\cos\psi - \cos\phi\sin\psi & \sin\phi\sin\psi + \cos\phi\sin\theta\cos\psi \\ \cos\theta\sin\psi & \cos\phi\cos\psi + \sin\phi\sin\theta\sin\psi & \cos\phi\sin\theta\sin\psi - \sin\phi\cos\psi \\ -\sin\theta & \sin\phi\cos\theta & \cos\phi\cos\theta \end{pmatrix}, \tag{9}$$

where $\mathbf{R}_s \in \Re^{3\times3}$ is the orthogonal rotation matrix from the non-inertial frame to the inertial frame. Based on this, the relative velocity of particle i should be $\mathbf{v}_i^r = \tilde{\mathrm{d}}\boldsymbol{\rho}_i \big/ \mathrm{d}t = \dot{x}_i\hat{\mathbf{e}}_x + \dot{y}_i\hat{\mathbf{e}}_y + \dot{z}_i\hat{\mathbf{e}}_z$, where we define $\tilde{\mathrm{d}}\boldsymbol{\rho}_i \big/ \mathrm{d}t$ as a relative derivative. As for the absolute velocity, it equals the summation of relative velocity $\tilde{\mathrm{d}}\boldsymbol{\rho}_i \big/ \mathrm{d}t$ and the cross product of angular velocity vector and position vector,

$$\mathbf{v}_i = \frac{\mathrm{d}\mathbf{r}_o}{\mathrm{d}t} + \boldsymbol{\Omega} \times \boldsymbol{\rho}_i + \frac{\tilde{\mathrm{d}}\boldsymbol{\rho}_i}{\mathrm{d}t}, \tag{10}$$

where the first two terms on the right side are usually termed transport velocity, and the last is relative velocity.

Taking the derivative of Eq. (10) with respect to t again, we can obtain the absolute acceleration of particle i:

$$\mathbf{a}_i = \frac{\tilde{\mathrm{d}}^2\boldsymbol{\rho}_i}{\mathrm{d}t^2} + 2\boldsymbol{\Omega}\times\frac{\tilde{\mathrm{d}}\boldsymbol{\rho}_i}{\mathrm{d}t} + \frac{\mathrm{d}^2\mathbf{r}_o}{\mathrm{d}t^2} + \dot{\boldsymbol{\Omega}}\times\boldsymbol{\rho}_i + \boldsymbol{\Omega}\times(\boldsymbol{\Omega}\times\boldsymbol{\rho}_i), \tag{11}$$

where $\tilde{\mathrm{d}}^2\boldsymbol{\rho}_i \big/ \mathrm{d}t^2$ is termed relative acceleration; $2\boldsymbol{\Omega}\times\tilde{\mathrm{d}}\boldsymbol{\rho}_i \big/ \mathrm{d}t$ is the Coriolis acceleration; and the last three terms together are transport acceleration. Except the relative acceleration, all other terms are related to the transformation of coordinates. Therefore, for a brief illustration we define these four terms as inertial acceleration, which should be regarded as a body acceleration in the SPH equations, that is

$$\mathbf{a}_i^{\text{inertial}} = 2\boldsymbol{\Omega}\times\frac{\tilde{\mathrm{d}}\boldsymbol{\rho}_i}{\mathrm{d}t} + \frac{\mathrm{d}^2\mathbf{r}_o}{\mathrm{d}t^2} + \dot{\boldsymbol{\Omega}}\times\boldsymbol{\rho}_i + \boldsymbol{\Omega}\times(\boldsymbol{\Omega}\times\boldsymbol{\rho}_i). \tag{12}$$

We substitute absolute acceleration with relative acceleration and inertial acceleration, and regard the inertial acceleration and gravity as the body acceleration. The momentum equation Eq. (1-b) then can be rewritten in the following form:

$$\frac{\tilde{\mathrm{d}}^2\boldsymbol{\rho}_i}{\mathrm{d}t^2} = -\sum\nolimits_j m_j\left(\frac{p_i}{\rho_i^2}+\frac{p_j}{\rho_j^2}\right)\nabla_i W_{ij} + \sum\nolimits_j \frac{4m_j(\mu_i+\mu_j)}{(\rho_i+\rho_j)^2} \times \frac{\boldsymbol{\rho}_{ij}\cdot\nabla_i W_{ij}}{|\boldsymbol{\rho}_{ij}|^2+0.01h^2}\cdot\mathbf{v}_{ij} + \mathbf{g} - \mathbf{a}_i^{\text{inertial}}, \tag{13}$$

where $\mathbf{v}_{ij} = \mathbf{v}_i - \mathbf{v}_j = \mathbf{v}_{ij}^r + \boldsymbol{\Omega}\times\boldsymbol{\rho}_{ij}$;$\mathbf{g} = -g\mathbf{e}_z = -9.81\mathbf{e}_z$.

2.3 Extraction of Sloshing Force and Sloshing Moment

Traditional methods for calculating the sloshing force or buoyancy force are usually realized by integrating the pressure along the surface [34, 43]. However, the fluctuation of the pressure field limits its application. Recently, a new method [43, 45] based on linear and angular momentum theorems was proposed and has been widely used for the calculation of sloshing force and moment. Regarding all the smoothed particles for flows inside the tank as a whole, the gravity $m_{\text{liquid}}\mathbf{g}$, inertial force $m_{\text{liquid}}\sum_i \mathbf{a}_i^{\text{inertial}}$, and contact force $\mathbf{F}_\text{N}$ are all the forces acting on the particle system. Note that the contact force and sloshing force $\mathbf{F}_\text{s}$ are a pair of interaction forces. Therefore, the sloshing force can be derived by solving the contact force.

The momentum $\mathbf{P}$ of all fluid particles is

$$\mathbf{P} = \sum\nolimits_i m_i\mathbf{v}_i. \tag{14}$$

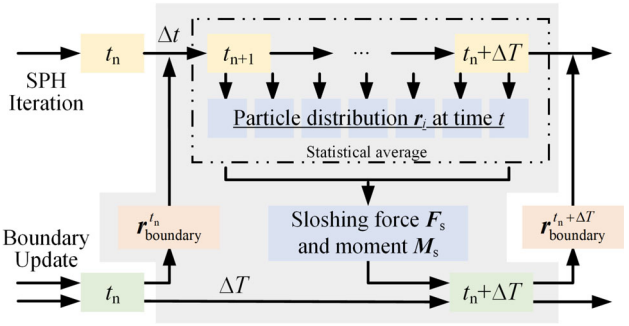

Fig. 3 Iteration for solving the liquid-filled UAV system by non-inertial SPH method

By linear momentum theory, we can derive

$$\frac{\mathrm{d}\mathbf{P}}{\mathrm{d}t} = \frac{\mathrm{d}}{\mathrm{d}t}\sum\nolimits_i m_i\mathbf{v}_i = \mathbf{F}_\text{N} + \mathbf{g}m_{\text{liquid}}. \tag{15}$$

That is,

$$\mathbf{F}_\text{s} = -\mathbf{F}_\text{N} = \sum\nolimits_i m_i(-\mathbf{a}_i^{\text{inertial}} + \mathbf{g}) - \frac{1}{\Delta T}\sum\nolimits_i m_i(\mathbf{v}_i^{r,t} - \mathbf{v}_i^{r,t-\Delta T}). \tag{16a}$$

The sloshing moment can be also obtained by a similar derivation, that is

$$\mathbf{M}_\text{s} = \sum\nolimits_i \boldsymbol{\rho}_i\times m_i(-\mathbf{a}_i^{\text{inertial}} + \mathbf{g}) - \frac{1}{\Delta T}\sum\nolimits_i \boldsymbol{\rho}_i\times m_i(\mathbf{v}_i^{r,t} - \mathbf{v}_i^{r,t-\Delta T}), \tag{16b}$$

where ΔT is the time step between two updates of the boundary conditions. At each time step of ISPH, the linear and angular momentums can be collected based on the dynamics information of particles. When the boundary update step comes, only the momentum data, which are within $\pm$ 3 standard deviations of the mean, are kept. The sloshing force and moment are then computed using the mean of the data.

Figure 3 shows the iteration framework of the proposed non-inertial ISPH method. Based on the latest boundary update results, the physical parameters of particles iterate step by step and finally export the sloshing force and moment for the boundary update in next time. The so-called boundary update, in fact, is the attitude adjustment of the liquid-filled quadrotor, which is studied in Sect. 3.

3 Dynamics and Control of the Liquid-Filled Quadrotor UAV

3.1 Modeling of the Quadrotor with Sloshing Load

The quadrotor itself and its operational environment might be very complex, and therefore the modeling could be feasible only based on some rational assumptions. Here we introduce the assumptions that our work is based on.

Assumption 1 *Ignore the dynamics of the DC motor and assume that the DC motor could reach the required rotating speed immediately because the advanced rotor now has excellent adjusting performance;*

Assumption 2 *Ignore the air drag force because the liquid-filled quadrotor moves in a low speed;*

Assumption 3 *The quadrotor usually has a symmetrical and large-stiffness structure, so assume that the quadrotor with an empty load is rigid and symmetrical with respect to all axes;*

Assumption 4 *When designing the controller, only the angular momentum of liquid gravity (no sloshing effect) is taken into consideration. If not, the computation cost would be considerable and real-time control would be impracticable.*

Define the state vector $\mathbf{X}$, which has 12 states of the quadrotor motion, as follows [47, 48]

$$\mathbf{X} = (x,\ \dot{x},\ y,\ \dot{y},\ z,\ \dot{z},\ \phi,\ p,\ \theta,\ q,\ \psi,\ r)^{\mathrm{T}}. \tag{17}$$

Based on assumption 1 and the Newton–Euler formulations, the quadrotor could be regarded as a 6-DOF rigid body and its dynamics differential equations are derived.

$$\dot{\boldsymbol{r}}_{\mathrm{o}} = \mathbf{v}_{\mathrm{o}}, \tag{18a}$$

$$m_{\mathrm{uav}}\dot{\boldsymbol{v}}_{\mathrm{o}} = m_{\mathrm{uav}}\mathbf{g} + T\mathbf{R}_{\mathrm{s}}\hat{\boldsymbol{e}}_{\mathrm{z}} + \mathbf{R}_{\mathrm{s}}\mathbf{F}_{\mathrm{s}}, \tag{18b}$$

$$\dot{\boldsymbol{R}}_{\mathrm{s}} = \mathbf{R}_{\mathrm{s}}\mathbf{S}(\boldsymbol{\Omega}), \tag{18c}$$

$$\mathbf{I}_{\mathrm{uav}}\dot{\boldsymbol{\Omega}} = -\boldsymbol{\Omega} \times \mathbf{I}_{\mathrm{uav}}\boldsymbol{\Omega} + \boldsymbol{\tau}^{\mathrm{a}} + \mathbf{M}_{s}, \tag{18d}$$

where $\mathbf{F}_{\mathrm{s}} = \mathrm{diag}(F_s^x,\ F_s^y,\ F_s^z)$ and $\mathbf{M}_{\mathrm{s}} = \mathrm{diag}(M_s^x,\ M_s^y,\ M_s^z)$ are the sloshing force and moment, respectively; m_{uav} and $\mathbf{I}_{\mathrm{uav}} = \mathrm{diag}(I_{uav}^x,\ I_{uav}^y,\ I_{uav}^z)$ denotes the quadrotor mass and momentum of the inertia matrix, respectively; $\mathbf{S}(\boldsymbol{\Omega})$, a skew-symmetric matrix, is defined as follows:

$$\mathbf{S}(\boldsymbol{\Omega}) = \begin{pmatrix} 0 & -r & q \\ r & 0 & -p \\ -q & p & 0 \end{pmatrix}. \tag{19}$$

T and $\boldsymbol{\tau}^{\mathrm{a}} = (\tau_1^a,\ \tau_2^a,\ \tau_3^a)^{\mathrm{T}}$ in Eq. (18) are the thrust produced by the four rotors, which are the total thrust force and control torques, respectively. The thrust of each rotor is proportional to its rotating speed, and the positive proportionality constants are k_{T} and k_{M}, which are related to the rotor blades, air density, pitch angle of blades, and so on. In order to facilitate the calculation of actual control inputs, these parameters are assembled as follows:

$$\begin{aligned} \mathbf{U} &= \begin{pmatrix} T \\ \tau_1^a \\ \tau_2^a \\ \tau_3^a \end{pmatrix} \\ &= \begin{pmatrix} k_{\mathrm{T}} & k_{\mathrm{T}} & k_{\mathrm{T}} & k_{\mathrm{T}} \\ 0 & -k_{\mathrm{T}}l_{\mathrm{uav}} & 0 & k_{\mathrm{T}}l_{\mathrm{uav}} \\ -k_{\mathrm{T}}l_{\mathrm{uav}} & 0 & k_{\mathrm{T}}l_{\mathrm{uav}} & 0 \\ -k_{\mathrm{M}}l_{\mathrm{uav}} & k_{\mathrm{M}}l_{\mathrm{uav}} & -k_{\mathrm{M}}l_{\mathrm{uav}} & k_{\mathrm{M}}l_{\mathrm{uav}} \end{pmatrix} \begin{pmatrix} \omega_1^2 \\ \omega_2^2 \\ \omega_3^2 \\ \omega_4^2 \end{pmatrix}. \end{aligned} \tag{20}$$

where l_{uav} is the distance between two rotor centers in the diagonal direction. ω_i ,where i equals 1, 2, 3, 4, are the rotating speeds of the four rotors.

Also, by a simple algebraic calculation, the angular velocity transformation matrices can be expressed as

$$\dot{\boldsymbol{\Theta}} = \dot{\mathbf{R}}_{\mathrm{w}}\boldsymbol{\Omega} = \begin{pmatrix} 1 & \sin\phi\tan\theta & \cos\phi\tan\theta \\ 0 & \cos\phi & -\sin\phi \\ 0 & \sin\phi\sec\theta & \cos\phi\sec\theta \end{pmatrix} \boldsymbol{\Omega}. \tag{21}$$

By substituting Eqs. (19–21) to Eq. 18, the overall dynamics model of the liquid-filled quadrotor under real-time control, $\dot{\mathbf{X}} = f(\mathbf{X})$, then can be expressed as follows:

$$\dot{\mathbf{X}} = \begin{pmatrix} \dot{x} \\ [F_s^x \cos\theta\cos\phi + F_s^y(-\cos\phi\sin\psi + \sin\phi\sin\theta\cos\psi) + (T + F_s^z)(\sin\phi\sin\psi + \cos\phi\sin\theta\cos\psi)]\big/ m_{\text{uav}} \\ \dot{y} \\ [F_s^x \cos\theta\sin\psi + F_s^y(\cos\phi\cos\psi + \sin\phi\sin\theta\sin\psi) + (T + F_s^z)(-\sin\phi\cos\psi + \cos\phi\sin\theta\sin\psi)]\big/ m_{\text{uav}} \\ \dot{z} \\ -g + [-F_s^x \sin\theta + F_s^y \sin\phi\cos\theta + (T + F_s^z)\cos\phi\cos\theta]\big/ m_{\text{uav}} \\ p + q\sin\phi\tan\theta + r\cos\phi\tan\theta \\ [qr(I_y - I_z) + \tau_1^a + M_s^x]\big/ I_x \\ q\cos\phi - r\sin\phi \\ [pr(I_z - I_x) + \tau_2^a + M_s^y]\big/ I_y \\ q\sin\phi\sec\theta + r\cos\phi\sec\theta \\ [pq(I_x - I_y) + \tau_3^a + M_s^z]\big/ I_z \end{pmatrix}. \tag{22}$$

3.2 Designing the Controller

A liquid-filled quadrotor is a typical under-actuated system, and its performance closely relies on the control algorithm, especially under the strong sloshing effect. In the classical flight control system, the analytic computation of derivative expression of command trajectory is quite intricate. To avoid this problem, in this section, the two-channel control method is applied; it consists of a position control channel based on PID and an attitude control channel based on backstepping control. Given the sudden change of the desired velocity and acceleration at the unsmooth curve, a second-order command filter is introduced to force states x, y, z, and ψ track the commanded references x_{d}, y_{d}, z_{d}, and ψ_{d}.

Due to the requirement of real-time control on board, based on assumption 4 only the liquid gravity is taken into consideration in the controller, which means that the dynamics model is changed to the following form:

$$m_{\text{uav}}\dot{\mathbf{v}}_{\text{o}} = m_{\text{uav}}\mathbf{g} + T\mathbf{R}_{\text{s}}\hat{\mathbf{e}}_{\text{z}} + m_{\text{liquid}}\mathbf{g}, \tag{23a}$$

$$\mathbf{I}_{\text{uav}}\dot{\boldsymbol{\Omega}} = -\boldsymbol{\Omega}\times\mathbf{I}_{\text{uav}}\boldsymbol{\Omega} + \boldsymbol{\tau}^{\text{a}} + \mathbf{M}_g, \tag{23b}$$

where $m_{\text{liquid}}\mathbf{g}$ and $\mathbf{M}_{\text{g}}$ are the gravity and gravity momentum of the liquid. $\mathbf{M}_{\text{g}}$ can be derived by regarding the liquid as a mass center,

$$\mathbf{M}_g = \mathbf{R}_{\text{s}}\boldsymbol{\rho}_{\text{ol}} \times m_{\text{liquid}}\mathbf{g}, \tag{24}$$

where $\boldsymbol{\rho}_{\text{ol}}$ is the position vector from origin o of the body-frame to the mass center of the liquid.

In our position control channel, first define the position error as

$$\mathbf{r}_{\text{e}} = \mathbf{r}_{\text{o}} - \mathbf{r}_{\text{c}}, \tag{25}$$

where $\mathbf{r}_{\text{c}} = (x_{\text{c}}, y_{\text{c}}, z_{\text{c}})^{\text{T}}$ is the commanded trajectory of the quadrotor. We construct the position PID equation as follows:

$$\ddot{\mathbf{r}}_{\text{e}} + \mathbf{K}_p\mathbf{r}_{\text{e}} + \mathbf{K}_i\int\mathbf{r}_{\text{e}}\text{d}t + \mathbf{K}_d\dot{\mathbf{r}}_{\text{e}} = 0, \tag{26}$$

where $\mathbf{K}_p$, $\mathbf{K}_i$, $\mathbf{K}_d$ are the control parameters of the PID controller, which are all positive definite matrices. Substituting Eqs. (25) into Eq. (26), we can obtain

$$\ddot{\mathbf{r}}_{\text{o}} = \ddot{\mathbf{r}}_{\text{c}} - \mathbf{K}_p(\mathbf{r}_{\text{o}} - \mathbf{r}_{\text{c}}) - \mathbf{K}_i\int(\mathbf{r}_{\text{o}} - \mathbf{r}_{\text{c}})\text{d}t - \mathbf{K}_d(\dot{\mathbf{r}}_{\text{o}} - \dot{\mathbf{r}}_{\text{c}}). \tag{27}$$

We define a virtual control input $\mathbf{U}_{\text{v}} = \ddot{\mathbf{r}}_{\text{o}} = (U_1, U_2, U_3)^{\text{T}}$. The $\dot{\mathbf{v}}_o$ term in Eq. (23-a) can then be replaced by $\mathbf{U}_{\text{v}}$,

$$\mathbf{R}_{\text{s}}^{-1}\left[\mathbf{U}_{\text{v}} - (1 + \frac{m_{\text{liquid}}}{m_{\text{uav}}})\mathbf{g}\right] = \frac{T}{m_{\text{uav}}}\hat{\mathbf{e}}_{\text{z}}. \tag{28}$$

Let $\kappa_{\text{m}} = m_{\text{liquid}}\big/ m_{\text{uav}}$. Considering the commanded yaw ψ_{c}, the commanded pitch angle θ_{c} and roll angle φ_{c} can be expressed as

$$\theta_{\text{c}} = \arctan\left(\frac{U_1\cos\psi_c + U_2\sin\psi_c}{U_3 + (1+\kappa_{\text{m}})g}\right), \tag{29a}$$

$$\phi_{\text{c}} = \arcsin\left(\frac{U_1\sin\psi_c - U_2\cos\psi_c}{\sqrt{U_1^2 + U_2^2 + [U_3 + (1+\kappa_{\text{m}})g]^2}}\right), \tag{29b}$$

In this process, the total thrust can also be derived as

$$\begin{aligned} T = m_{\text{uav}}\{&U_1(\cos\phi\sin\theta\cos\psi + \sin\phi\sin\psi) \\ &+U_2(\cos\phi\sin\theta\sin\psi - \sin\phi\cos\psi) \\ &+[U_3 + (1+\kappa_{\text{m}})g]\cos\phi\cos\theta\}. \end{aligned} \tag{30}$$

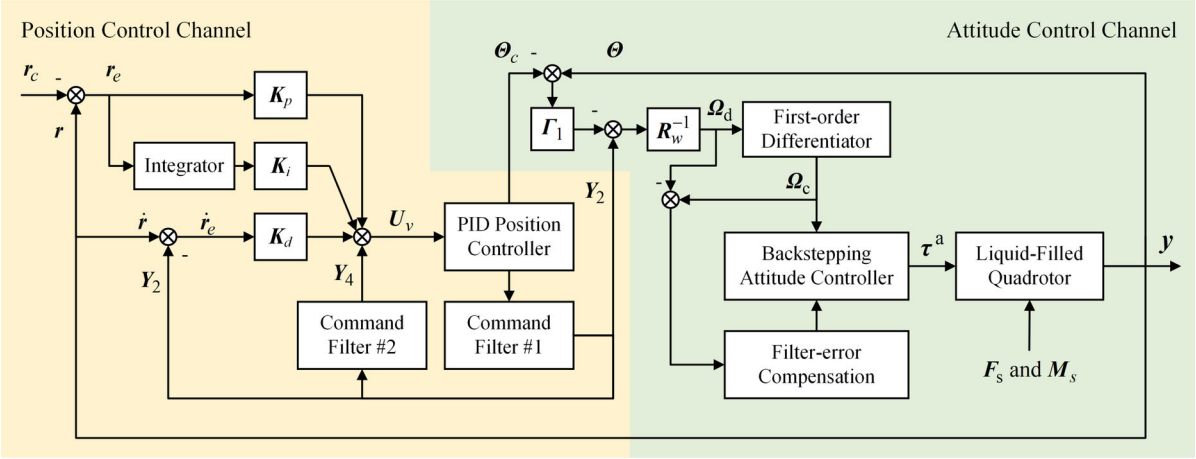

Fig. 4 Block diagram of the control algorithm for the liquid-filled quadrotor UAV

Similar to Eq. (25), the attitude error and angular velocity error can also be defined as

$$\boldsymbol{\Theta}_{\mathrm{e}} = \boldsymbol{\Theta} - \boldsymbol{\Theta}_{\mathrm{c}}, \tag{31}$$

$$\boldsymbol{\Omega}_{\mathrm{e}} = \boldsymbol{\Omega} - \boldsymbol{\Omega}_{\mathrm{c}}, \tag{32}$$

where $\boldsymbol{\Theta}_{\mathrm{c}} = (\phi_{\mathrm{c}}, \theta_{\mathrm{c}}, \psi_{\mathrm{c}})^{\mathrm{T}}$ and $\boldsymbol{\Omega}_{\mathrm{c}}$ are the references of the attitude angle and angular velocity, respectively. Consider the following Lyapunov function [47, 48]:

$$V_1 = \frac{1}{2}\boldsymbol{\Theta}_{\mathrm{e}}^{\mathrm{T}}\boldsymbol{\Theta}_{\mathrm{e}}. \tag{33}$$

Taking the time derivative of Eq. (33) yields

$$\dot{V}_1 = \boldsymbol{\Theta}_{\mathrm{e}}^{\mathrm{T}}\dot{\boldsymbol{\Theta}}_{\mathrm{e}} = \boldsymbol{\Theta}_{\mathrm{e}}^{\mathrm{T}}\left(\mathbf{R}_{\mathrm{w}}\boldsymbol{\Omega} - \dot{\boldsymbol{\Theta}}_{\mathrm{c}}\right). \tag{34}$$

We then consider a desired angular velocity

$$\boldsymbol{\Omega}_{\mathrm{d}} = \mathbf{R}_{\mathrm{w}}^{-1}(\dot{\boldsymbol{\Theta}}_{\mathrm{c}} - \boldsymbol{\Gamma}_1\boldsymbol{\Theta}_{\mathrm{e}}), \tag{35}$$

satisfies that matrix $\boldsymbol{\Gamma}_1$ is a positive definite matrix. If the angular velocity $\boldsymbol{\Omega}$ could track $\boldsymbol{\Omega}_{\mathrm{d}}$, then the negative definite characteristic $\dot{V}_1 < 0$ can be guaranteed,

$$\dot{V}_1 = -\boldsymbol{\Theta}_{\mathrm{e}}^{\mathrm{T}}\Gamma_1\boldsymbol{\Theta}_{\mathrm{e}}. \tag{36}$$

The negativeness of $\dot{V}_1$ means that the control of the attitude angle could be stable. However, to realize Eq. 35 without tedious mathematics derivation, a linear tracking differentiator is adopted to enforce the tracking of $\boldsymbol{\Omega}_{\mathrm{d}}$

$$\dot{\boldsymbol{\Omega}}_{\mathrm{c}} = -\overline{\mathrm{T}}(\boldsymbol{\Omega}_{\mathrm{c}} - \boldsymbol{\Omega}_{\mathrm{d}}), \tag{37}$$

where $\overline{\mathrm{T}}$ is also a positive definite matrix to ensure stability.

It should be noted that the tracking of derivatives of the commanded trajectories in Eqs. (27) and (34) might be difficult. The commanded trajectory is not always smooth, and sometimes even not continuous, and its derivative and second-order derivative can be considerable. Two cascaded second-order command filters are introduced here, which could circumvent the problem mentioned above [47–49]:

$$\begin{cases} \dot{\mathbf{Y}}_1 = \mathbf{Y}_2 \\ \dot{\mathbf{Y}}_2 = -2\boldsymbol{\Lambda}_1\mathbf{Y}_2 - \boldsymbol{\Lambda}_1^2(\mathbf{Y}_1 - \mathbf{X}_{\mathrm{c}}) \\ \dot{\mathbf{Y}}_3 = \mathbf{Y}_4 \\ \dot{\mathbf{Y}}_4 = -2\boldsymbol{\Lambda}_2\mathbf{Y}_4 - \boldsymbol{\Lambda}_2^2(\mathbf{Y}_3 - \mathbf{Y}_2). \end{cases} \tag{38}$$

where $\boldsymbol{\Lambda}_1$ and $\boldsymbol{\Lambda}_2$ are two positive definite matrices.$\mathbf{X}_{\mathrm{c}} = (x_c, y_c, z_c, \phi_c, \theta_c, \psi_c)^{\mathrm{T}}$ is a state vector with six states of the commanded trajectory of the quadrotor. Now the derivatives of the commanded trajectory in Eq. (27) and Eq. (34) can be replaced by $\mathbf{Y}_2$ and $\mathbf{Y}_4$.

The command filter Eq. (38) would cause tracking error, and therefore error compensation is required.

$$\dot{\boldsymbol{\varepsilon}} = -\boldsymbol{\Gamma}_1\boldsymbol{\varepsilon} + \mathbf{R}_{\mathrm{w}}(\boldsymbol{\Omega}_{\mathrm{c}} - \boldsymbol{\Omega}_{\mathrm{d}}). \tag{39}$$

Therefore, a new attitude error is redefined here.

$$\overline{\boldsymbol{\Theta}}_{\mathrm{e}} = \boldsymbol{\Theta}_{\mathrm{c}} - \boldsymbol{\varepsilon} = \boldsymbol{\Theta} - \boldsymbol{\Theta}_{\mathrm{c}} - \boldsymbol{\varepsilon}. \tag{40}$$

Subsequently, a new Lyapunov function is chosen:

$$V_2 = \frac{1}{2}\overline{\boldsymbol{\Theta}}_{\mathrm{e}}^{\mathrm{T}}\overline{\boldsymbol{\Theta}}_{\mathrm{e}} + \frac{1}{2}\boldsymbol{\Omega}_{\mathrm{e}}^{\mathrm{T}}\boldsymbol{\Omega}_{\mathrm{e}}. \tag{41}$$

Taking the time derivative of Eq. (41), we can derive the following:

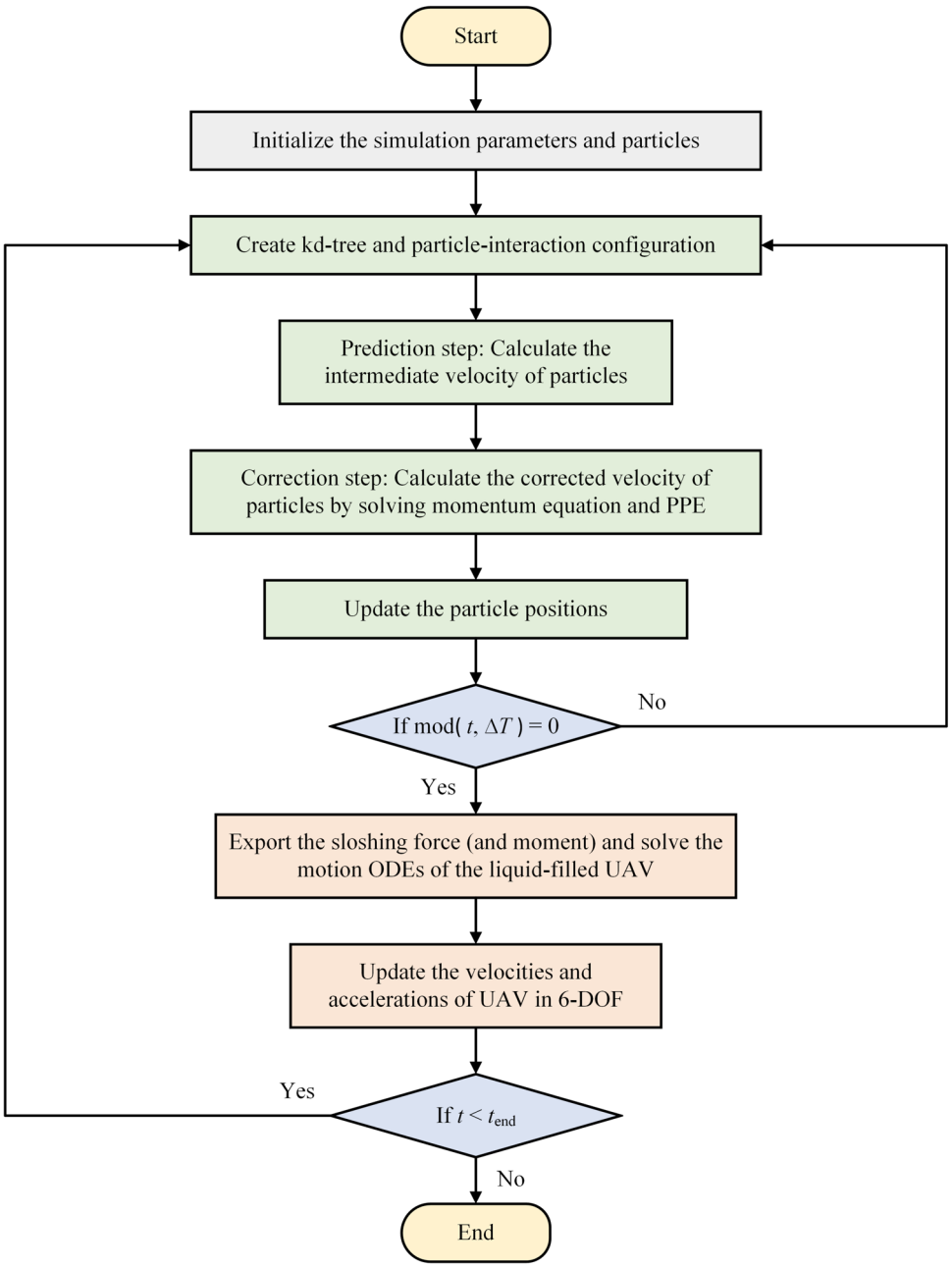

Fig. 5 Flowchart of coupled attitude/liquid/control simulation by non-inertial SPH method

$$\begin{aligned}\dot{V}_2 &= \boldsymbol{\Theta}_{\mathrm{e}}^{\mathrm{T}}\dot{\boldsymbol{\Theta}}_{\mathrm{e}} + \boldsymbol{\Omega}_{\mathrm{e}}^{\mathrm{T}}\dot{\boldsymbol{\Omega}}_{\mathrm{e}} \\ &= -\overline{\boldsymbol{\Theta}}_{\mathrm{e}}^{\mathrm{T}}\boldsymbol{\Gamma}_1\overline{\boldsymbol{\Theta}}_{\mathrm{e}} + \boldsymbol{\Omega}_{\mathrm{e}}^{\mathrm{T}}(-\mathbf{I}_{\mathrm{uav}}^{-1}\mathbf{S}\mathbf{I}_{\mathrm{uav}}\boldsymbol{\Omega} + \mathbf{I}_{\mathrm{uav}}^{-1}\mathbf{M}_g \\ &\quad + \mathbf{I}_{\mathrm{uav}}^{-1}\boldsymbol{\tau}^{\mathrm{a}} - \dot{\boldsymbol{\Omega}}_{\mathrm{c}} + \mathbf{R}_{\mathrm{w}}^{\mathrm{T}}\overline{\boldsymbol{\Theta}}_{\mathrm{e}}).\end{aligned} \tag{42}$$

To guarantee the stability by enforcing $\dot{V}_2 < 0$, the control torque $\boldsymbol{\tau}^{\mathrm{a}}$ can be chosen as

$$\begin{aligned}\boldsymbol{\tau}^{\mathrm{a}} &= \mathbf{S}\mathbf{I}_{\mathrm{uav}}\boldsymbol{\Omega} - \mathbf{M}_g + \mathbf{I}_{\mathrm{uav}}\overline{\mathrm{T}}\mathbf{R}_{\mathrm{w}}^{-1}\mathbf{Y}_2 - \mathbf{I}_{\mathrm{uav}}\overline{\boldsymbol{T}\boldsymbol{\Omega}}_{\mathrm{c}} - \mathbf{I}_{\mathrm{uav}}\overline{\mathrm{T}}\mathbf{R}_{\mathrm{w}}^{-1} \\ &\quad \times \boldsymbol{\Gamma}_1(\boldsymbol{\Theta} - \boldsymbol{\Theta}_{\mathrm{c}}) - \mathbf{I}_{\mathrm{uav}}\mathbf{R}_{\mathrm{w}}^{\mathrm{T}} \\ &\quad \times (\boldsymbol{\Theta} - \boldsymbol{\Theta}_{\mathrm{c}} - \boldsymbol{\varepsilon}) - \mathbf{I}_{\mathrm{uav}}\boldsymbol{\Gamma}_2(\boldsymbol{\Omega} - \boldsymbol{\Omega}_{\mathrm{c}}).\end{aligned} \tag{43}$$

Submit Eq. (43) into Eq. (42) we could find that the negativeness of $\dot{V}_2$ could be guaranteed by choosing two positive define matrices, $\boldsymbol{\Gamma}_1$ and $\boldsymbol{\Gamma}_2$

$$\dot{V}_2 = -\overline{\boldsymbol{\Theta}}_{\mathrm{e}}^{\mathrm{T}}\boldsymbol{\Gamma}_1\overline{\boldsymbol{\Theta}}_{\mathrm{e}} - \boldsymbol{\Omega}_{\mathrm{e}}^{\mathrm{T}}\boldsymbol{\Gamma}_2\boldsymbol{\Omega}_{\mathrm{e}}^{\mathrm{T}}. \tag{44}$$

Now the design of control inputs T and $\boldsymbol{\tau}^{\mathrm{a}}$ is finished, as Eq. (30) and Eq. (43) show. A block diagram of the proposed control algorithm for the liquid-filled quadrotor based on the constant-load hypothesis is shown in Fig. 4.

3.3 An Overview of the Proposed Attitude-Liquid-Control Algorithm

The previous subsections introduce the proposed attitude-liquid-control coupled simulation algorithms. As we can see, the simulation mainly consists of two parts, the CFD part and the flight dynamics part. The link that connects the two parts is the attitude of the quadrotor, as shown in Fig. 1. The liquid on board is modeled and simulated by the SPH method, as explained in Sect. 2. The control of the quadrotor is realized in this section. Figure 3 presents the iteration framework between them. The boundary of the fluid (or quadrotor attitude) is updated after every $\Delta T / \Delta t$ steps of the fluid particle updating until the simulation terminates. Figure 5 shows a flowchart of the attitude/liquid/control coupled algorithm by the non-inertial SPH method.

4 Dynamics Performance Analysis of the Liquid-Filled Quadrotor

4.1 Parameters of the 3D Maneuvering Flight

The working environment of a quadrotor is complex, and here a waypoint trajectory is chosen to test the proposed algorithm for the liquid-filled quadrotor. The waypoint trajectory is one of the most common trajectories in engineering operation, which is continuous but not smooth at the turning point. This problem can be solved well by the tracking differentiator proposed in Eq. (38). The commanded trajectory in this case is

Table 1 Simulation parameters of the liquid-filled quadrotor in 3-D maneuvering flight environment

Quadrotor physical parameters			
Mass of quadrotor m_{uav}	0.5 kg	Moment of inertia $\boldsymbol{I}_{\text{uav}}$	$5.2*10^{-3}$ kg·m^2, $5.2*10^{-3}$ kg·m^2, $9.3*10^{-3}$ kg·m^2
Distance between two rotors l_{uav}	0.225 m	Proportionality constants k_{T}, k_{M}	$2.98*10^{-6}$, $1.14*10^{-7}$
Height of liquid	0.05 m	Dimensions of liquid tank	0.1*0.1*0.1 m^3
Mass of liquid m_{liquid}	0.5 kg	Kinematic viscosity of liquid μ	$1.0*10^{-6}$ m^2/s
SPH parameters			
Number of particles	44,904	SPH numerical time step of Δt	$1*10^{-5}$ s
Simulation time t_{end}	10.0 s	Attitude updating time step ΔT	$1*10^{-3}$ s
Initial particle spacing dx	3.3 mm	Smooth length h	1.23*dx
Controller parameters			
$\mathbf{K}_p = 3\mathbf{E}_{3\times3}$	$\mathbf{K}_i = 2\mathbf{E}_{3\times3}$	$\mathbf{K}_d = 2\mathbf{E}_{3\times3}$	$\overline{\mathrm{T}} = 15\mathbf{E}_{3\times3}$
$\boldsymbol{\Gamma}_1 = 0.1\mathbf{E}_{3\times3}$	$\boldsymbol{\Gamma}_2 = 0.1\mathbf{E}_{3\times3}$	$\boldsymbol{\Lambda}_1 = 10\mathbf{E}_{6\times6}$	$\boldsymbol{\Lambda}_2 = 10\mathbf{E}_{6\times6}$

$$\begin{cases} x_c = 0 \cdot \text{fsg}(t,\ 0,\ 2) + (0.5t - 1) \cdot \text{fsg}(t,\ 2,\ 4) + (-0.5t + 3) \cdot \text{fsg}(t,\ 4,\ 6) + 0 \cdot \text{fsg}(t,\ 6,\ 10) \\ y_c = 0.5t \cdot \text{fsg}(t,\ 0,\ 2) + 1 \cdot \text{fsg}(t,\ 2,\ 4) + (-0.5t + 3) \cdot \text{fsg}(t,\ 4,\ 6) + 0 \cdot \text{fsg}(t,\ 6,\ 10) \\ z_c = 0.5t \cdot \text{fsg}(t,\ 0,\ 2) + 1 \cdot \text{fsg}(t,\ 2,\ 4) + (-0.5t + 3) \cdot \text{fsg}(t,\ 4,\ 6) + 0 \cdot \text{fsg}(t,\ 6,\ 10) \\ \psi_c = 0 \cdot \text{fsg}(t,\ 0,\ 10), \end{cases} \tag{45}$$

where fsg above is an interval function:

$$\text{fsg}(t,\ a,\ b) = \frac{\text{sign}(t - a) - \text{sign}(t - b)}{2}.$$

Table 1 shows the simulation parameters of the 3D maneuvering flight, including quadrotor physical parameters, SPH parameters, and controller parameters. Simulation results based on these parameters, where matrix $\mathbf{E}$ in the table means the identity matrix, are analyzed in Sect. 4.2.

4.2 Analysis and Discussion

The dynamics performance of the liquid-filled quadrotor in the 3-D maneuvering environment, simulated by the algorithm proposed above, is studied in this subsection. Figures 6–13 provide the quantitative results. Not only the quadrotor with sloshing liquid but also the empty load and constant load are investigated for comparison to see how sloshing influences the system.

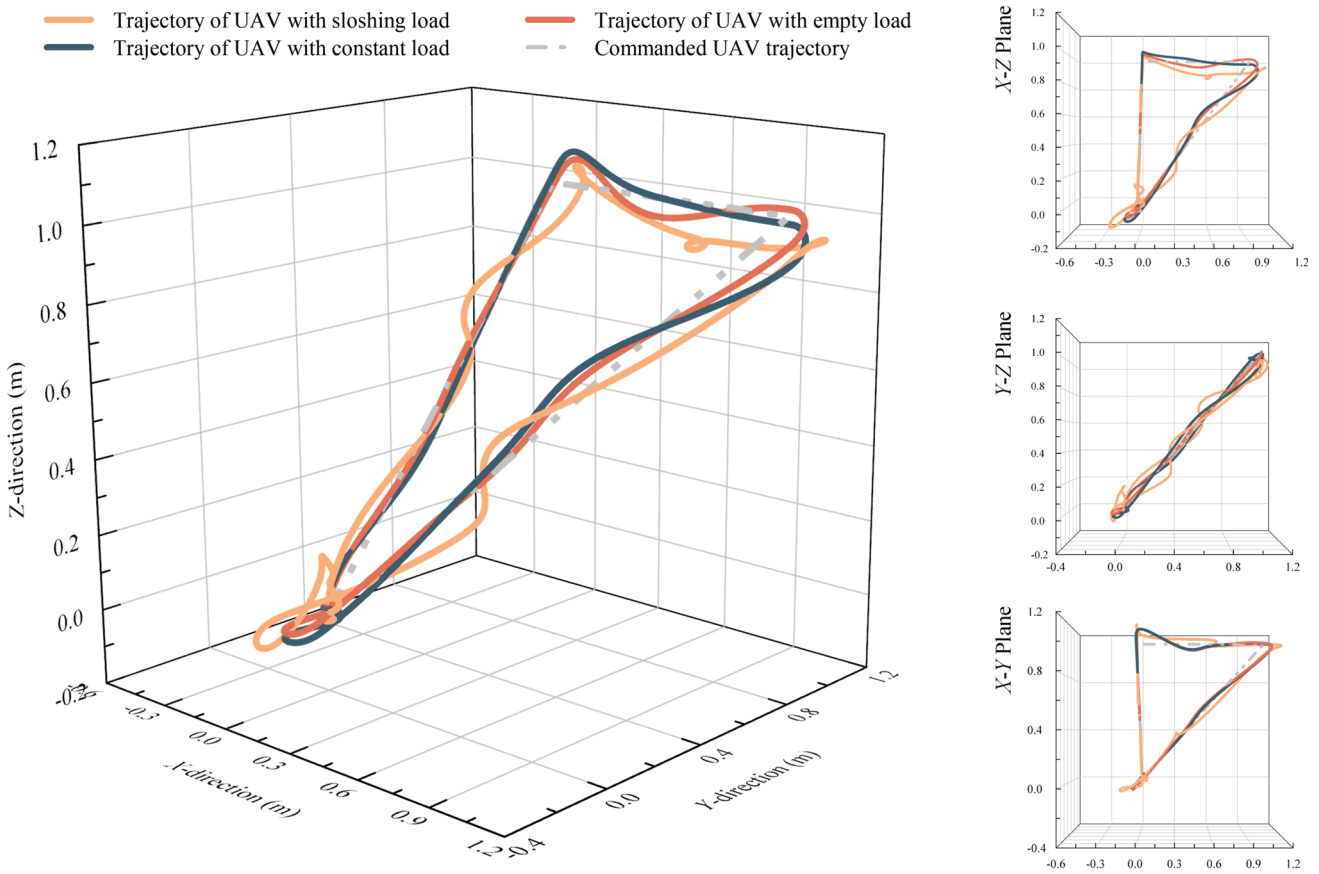

Fig. 6 3-D maneuvering flight trajectories of the UAV

Figure 6 shows the 3-D trajectories of the quadrotor in different view directions in these three cases, together with the commanded trajectory. As shown in the figure, the commanded trajectory is a space curve consisting of three straight lines. The quadrotor first takes off from the origin of the inertial frame, then passes through two points, and finally moves back to the origin and keeps hovering for a while. In Fig. 6, it can be easily observed that all three cases could realize the tracking of commanded trajectory, but the tracking performances are quite different. The responses, both the overshoot and the convergence speed, in the empty load and constant-load cases have an obviously lower overshoot. The differences between the constant case and the empty load case are limited, mainly appearing in vertical direction. To quantitative analyze the responses in different directions, Fig. 7 shows the results as given in Fig. 6 and the errors to the commanded trajectory in different directions. A summary of maximum overshoots of trajectory tracking in different directions under three cases are presented in Table 2. A noteworthy observation is that the effect of sloshing indeed has a significant effect on both the X-direction and Y-direction. Errors in the vertical direction are smaller than those in other directions, which means the anti-swing ability of the quadrotor is much weaker than that in the vertical direction.

The anti-swing ability is closely related to the responses of attitude angles [50–57]. To study the anti-swing ability, Fig. 8 shows the attitude angles in different directions during the maneuvering. The conclusion above is verified again by the results here. Notably, the principle of the quadrotor is the attitude adjustment by the rotating speed of the rotors to acquire the translational acceleration. The sloshing effect deteriorate the performance of the attitude angles, and inevitably lead to unsatisfactory tracking accuracy. From the results in Fig. 8, the maximum value of roll angle and pitch angle of the liquid-filled quadrotor are both around 0.25 rad. But in empty load and constant-load case, the values are only 0.05 rad and 0.10 rad, respectively. The reasons why values in empty load case is higher than constant-load case could be explained in two ways. The first reason is that the lighter quadrotor usually has an obvious overshoot than heavier quadrotor under the same control system. And it should also be noted that the center of gravity of the load is below the geometry center of the quadrotor, which provides a gravity angular stiffness to make the quadrotor easier keep stable [58, 59].

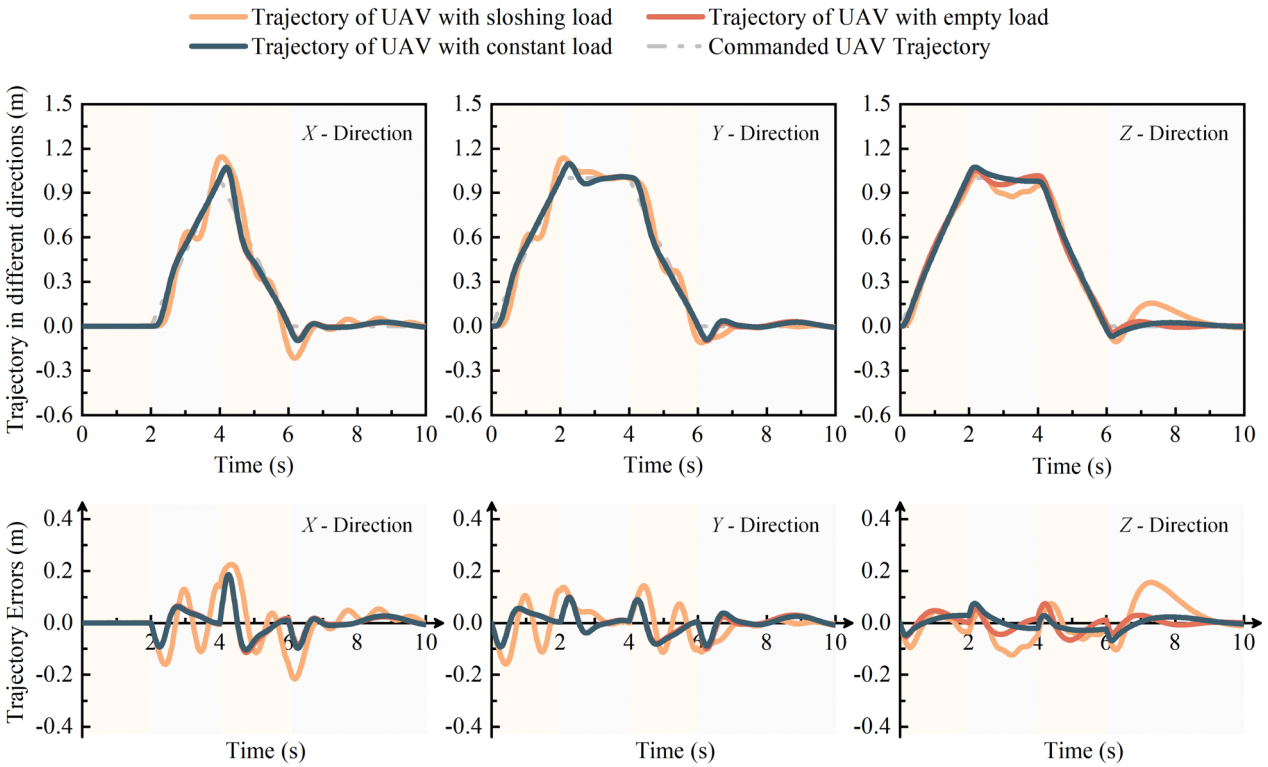

Fig. 7 The actual outputs of positions and their errors of the UAV in different directions

Table 2 Maximum overshoot of trajectory tracking in different directions under different load cases

	Taking-Off ($t = 2$ s)			Hovering ($t = 6$ s)		
	Sloshing load	Empty load	Constant load	Sloshing load	Empty load	Constant load
X—Direction	14.4%	7.3%	7.3%	21.6%	9.6%	9.6%
Y—Direction	13.7%	9.7%	9.7%	11.1%	9.9%	8.8%
Z—Direction	14.0%	5.4%	7.5%	15.6%	4.1%	6.7%

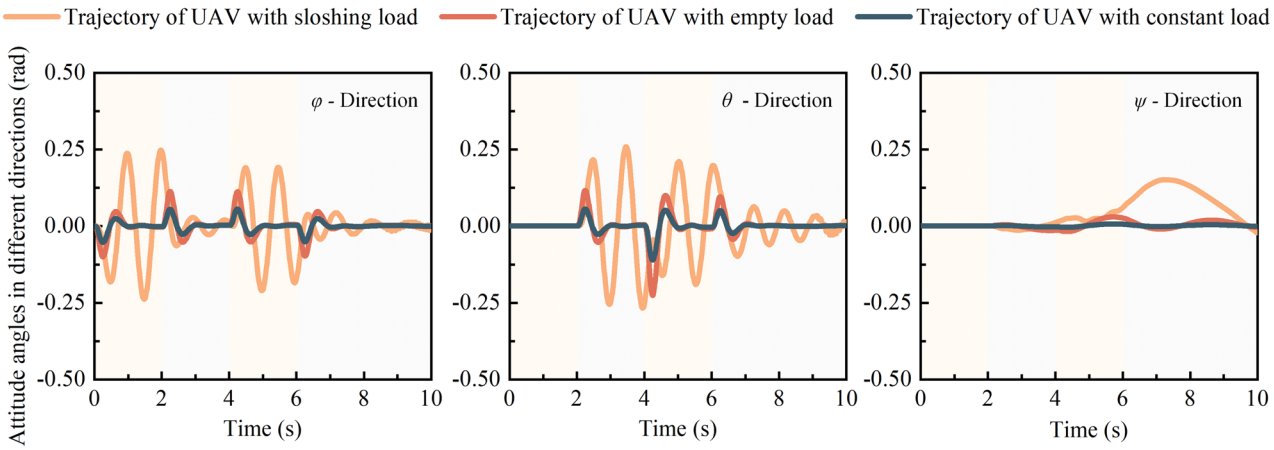

Fig. 8 The actual outputs of attitude angles of the UAV in different directions

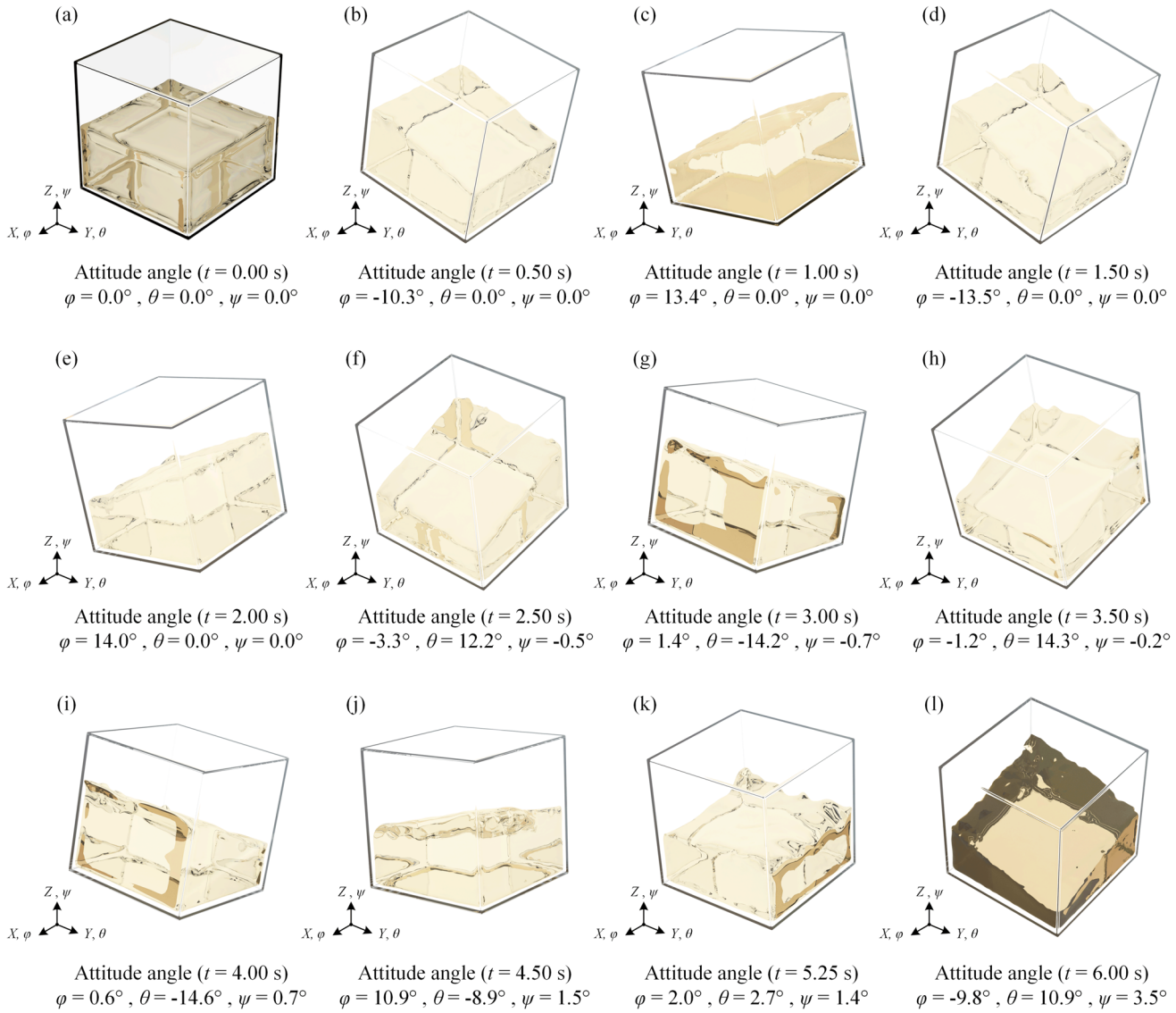

Fig. 9 Free surfaces of the liquid in the tank of UAV at different time

According to Eq. 45, the commanded yaw angle should be zero. From Fig. 8, the yaw angles under sloshing load, empty load, constant-load cases are 0.15 rad, 0.03 rad, and 0.0075 rad, respectively. The maximum yaw angle appears during hovering. At this time, the quadrotor just finishes its spatial trajectory tracking motion, which generates the vortex flow in tank. Therefore the tracking error of yaw angle mainly caused by the disturbance by sloshing torque in yaw direction. And this disturbance is hard to compensate by involving the constant load and empty load cases.

For the attitude adjustment, the attitude angles of the liquid-filled tank frequently change. To study the flow of water, especially the deformation of free-surface, the point cloud technology is applied based on the results by SPH algorithm. The attitudes of the liquid-filled quadrotor and the free-surfaces of liquid on board are displayed in Fig. 9. By the positions of smoothed particles, the point cloud could be utilized to generate meshes and then renderings at different times, as shown in the figure. The attitude and sloshing are apparently coupled and the deformation of free-surfaces is decided by the quadrotor attitude, which is also under the influence of sloshing.

The translational velocity and rotational velocity are shown in Figs. 10 and 11. Another noteworthy observation here is the 'inverse motion'. The commanded motion of quadrotor in Y-direction, as an example, should keep 0.5 m/s during—~ 2 s. It is normal that the real output slightly vibrates around the commanded value, but it could be observed during 1.11 s to 1.34 s, the velocity turns to be negative, which is the 'inverse motion' mentioned above. This phenomenon is

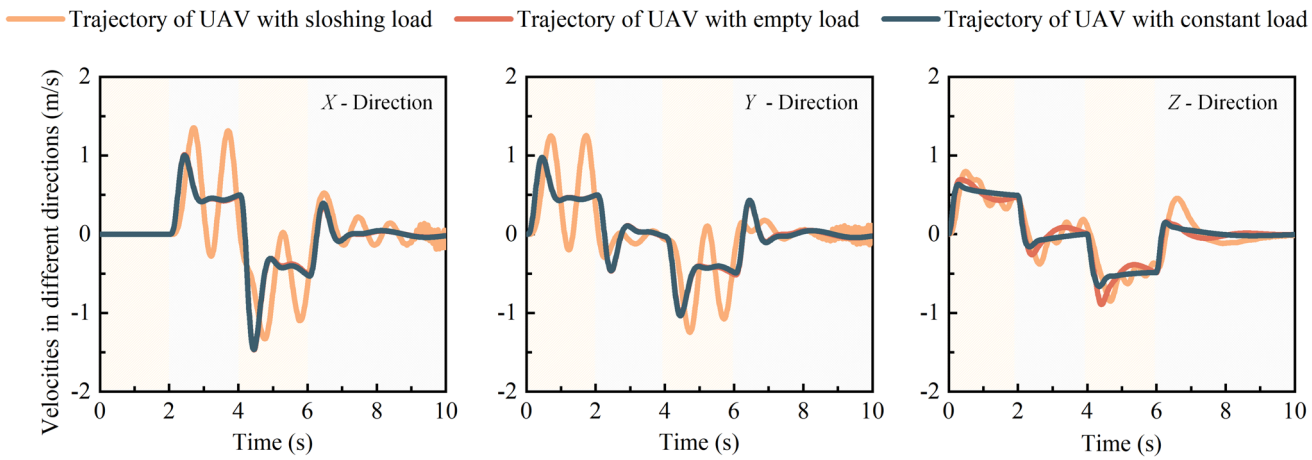

Fig. 10 The actual outputs of velocities of the UAV in different directions

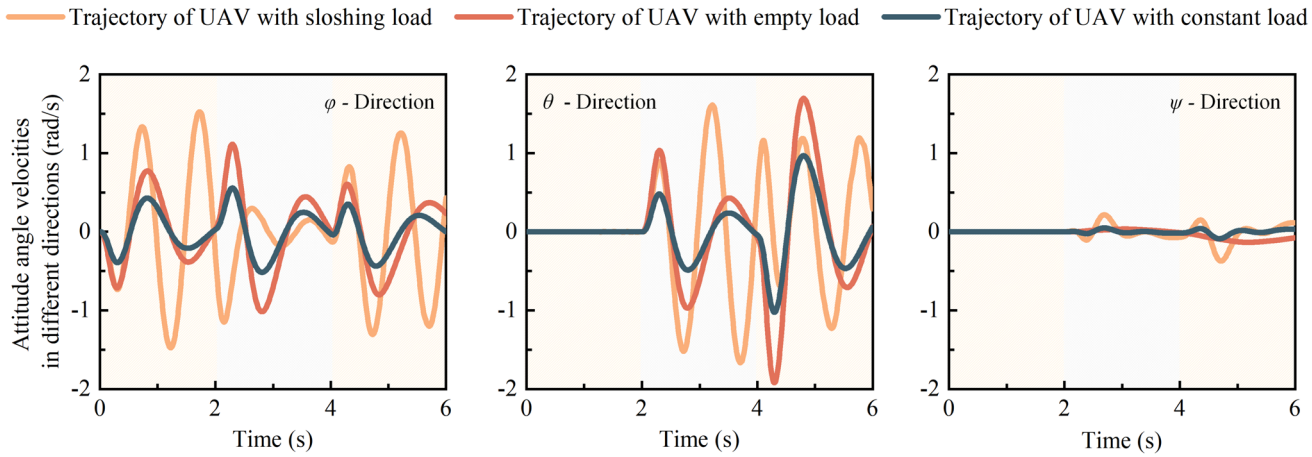

Fig. 11 The actual outputs of angle velocities of the UAV in different directions

caused by the violent sloshing in tank, and it is an unreasonable motion during the tracking task. Similar phenomenon also appears during 3.08 s to 3.34 s. Therefore, the liquid sloshing should be regarded as a important and key disturbance to the flight of liquid-filled quadrotor.

The rotating velocities of rotors of the liquid-filled quadrotor are presented in Fig. 12. Results under three cases show similar characteristics, which are closely related to the commanded trajectory tracking. At beginning, four rotors speed up to realize the taking-off. At $t = 2$ s and 4 s, rotors slow down to obtain the acceleration in negative vertical direction. After $t = 6$ s, four rotors shortly speed up to keep hovering. There are also two differences among three cases. The first one is that the rotating speed in empty load case (641 rpm) is obviously slower than the other two cases (907 rpm), this is because of the difference of taking-off mass. Moreover, for the sloshing effect, the rotating speed of rotors in sloshing load case vibrates more violent than the other two cases. The fluctuation of rotating speed is both the reason and result of the attitude instability.

The sloshing force in three different direction are shown in Fig. 13. As shown in figure, the amplitude of sloshing forces in horizontal direction is around 1 N. In vertical direction, the sloshing force is about 4.85 $\pm$ 0.1 N. That is, in this case an approximate estimation could be obtained that the sloshing force in horizontal direction is around 20% of the liquid gravity, and in vertical direction the variation is less than 5% of its gravity. This also accounts for the smaller tracking errors of the UAV position in the vertical direction, as Fig. 7 shows.

5 Conclusions

The simulation of fluid–structure interaction under active control is difficult owing to its complexity. For the simulation of attitude-liquid-control coupled dynamics of a liquid-filled quadrotor in a 3-D maneuvering environment, this paper proposed an algorithm on the basis of an iteration framework between a SPH simulation and the flight dynamics.

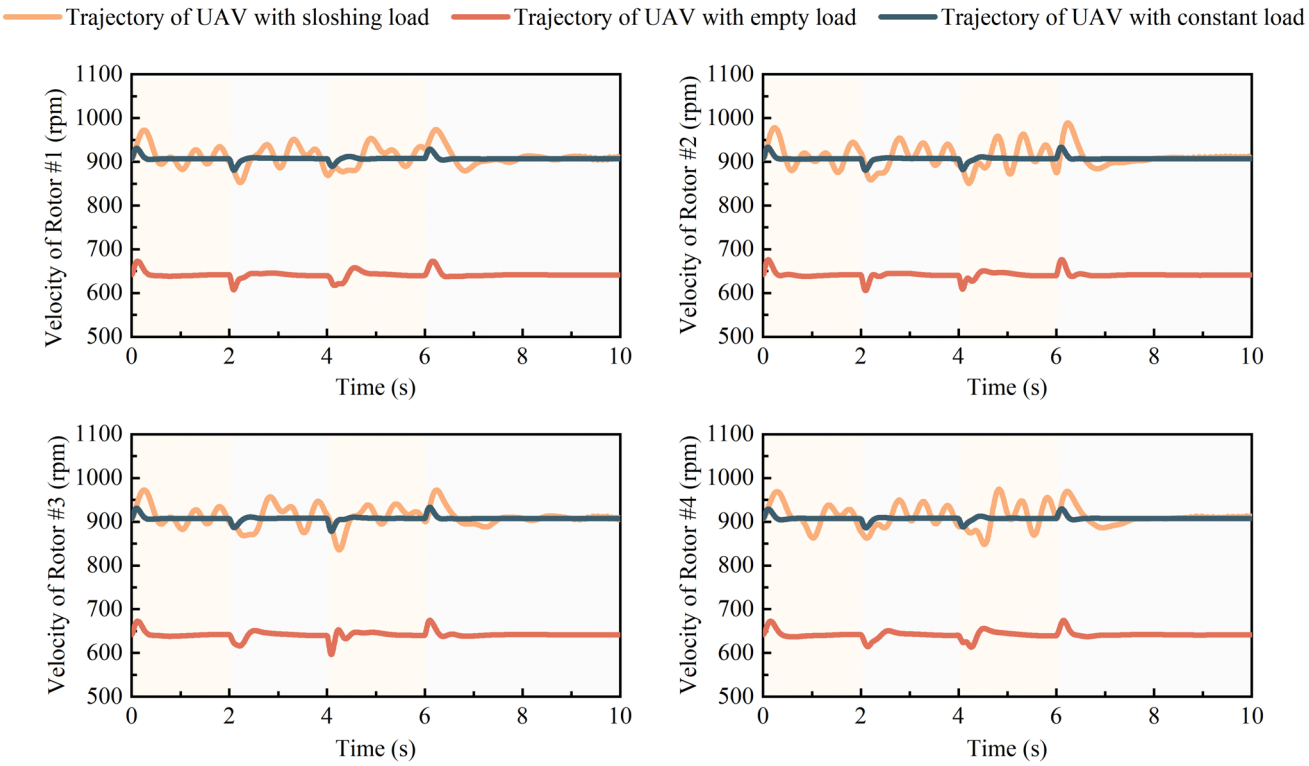

Fig. 12 Time history of the rotating velocities of the liquid-filled UAV rotors

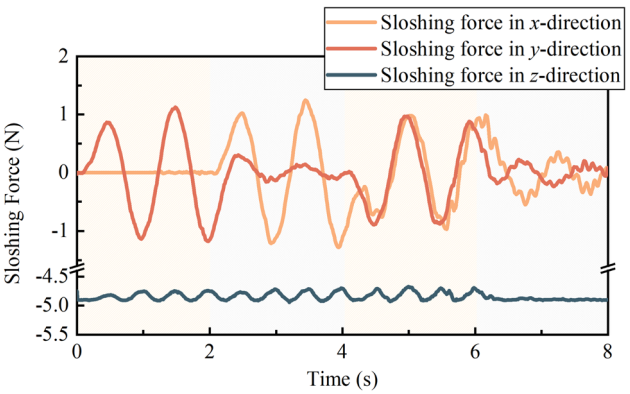

Fig. 13 Sloshing force by the non-inertial SPH method in the liquid-filled UAV system in 3-D maneuvering environment

The SPH method deployed in this paper is non-inertial SPH, and the sloshing forces and moments are extracted by the linear and angular momentum theorems of the particle system. A PID + backstepping controller is designed for stability of the quadrotor. The whole algorithm is tested and validated by comparison with two other cases. The dynamics performance of the liquid-filled quadrotor is also studied and analyzed in this work. The following conclusions could be obtained from the results:

1. During maneuvering, the effect of liquid sloshing to the trajectory tracking is negative. The sloshing force and torque disturb the equilibrium of quadrotor and then the adjustment of rotor speed makes the attitude tilt, which exacerbates the sloshing in tank. This phenomenon is more prominent in horizontal direction than vertical direction;

2. The effect of liquid sloshing has two opposing characteristics. When the liquid-filled quadrotor is moving and maneuvering, the liquid sloshing deteriorates the performance of tracking accuracy. But when the quadrotor stops to hover, the liquid gravity provides an angular gravity stiffness and stabilizes the attitude in a short time;

3. The amplitudes of sloshing forces in the X-direction and Y-direction are about 20% of liquid gravity, and in the vertical direction the proportion is less than 5%. This also accounts for the fact that the tracking error in the vertical direction is less than that in the horizontal direction.

Acknowledgements This work is supported by the National Natural Science Foundation of China (No. 12302051), China Postdoctoral Science Foundation (No. 2023M742542), and the Postdoctoral Fellowship Program of CPSF under grant number GZB20230503. The first author is grateful for the financial support from China Scholarship Council (No. 202006120119).

Data availability The data that support the findings of this study are available from the corresponding authors upon reasonable request.

Declarations

Conflict of interest The authors declare that they have no conflict of interest.

References

1. Jeong H, Suk J, Kim S, Lee Y, Cho T, Jeong J (2024) Aerodynamic Modeling and Verification of Quadrotor UAV Using Wind-Tunnel Test. Int J Aeronaut Space Sci 25:809–835
2. Kim C, Ji C, Koh G, Choi N (2024) Review on Flight Control Law Technologies of Fighter Jets for Flying Qualities. Int J Aeronaut Space Sci 24:209–236
3. H. Hassani, A. Mansouri, A. Ahaitouf, Model-Based Robust Tracking Attitude and Altitude Control of an Uncertain Quadrotor Under Disturbances, Int. J. Aeronaut. Space Sci. (2024).
4. Bui DN, Nguyen TTV, Phung MD (2023) Lyapunov-Based Nonlinear Model Predictive Control for Attitude Trajectory Tracking of Unmanned Aerial Vehicles. Int J Aeronaut Space Sci 24:502–513
5. Gerrits J, Veldman AEP (2003) Dynamics of liquid-filled spacecraft. J Eng Math 45:21–38
6. Y. Feng, C. A. Rabbath, C. Su, Modeling of a micro UAV with slung payload, Springer, (2015) 1257–1272.
7. Cao Y, Nie W, Wang Z, Wan S (2020) Dynamic modeling of helicopter-slung load system under the flexible sling hypothesis. Aerosp Sci Technol 99:105770
8. Sayyaadi H, Soltani A (2018) Modeling and control for cooperative transport of a slung fluid container using quadrotors. Chin J Aeronaut 31:262–272
9. Liu D, Lin P (2009) Three-dimensional liquid sloshing in a tank with baffles. Ocean Eng 36:202–212
10. Liu D, Lin P (2008) A numerical study of three-dimensional liquid sloshing in tanks. J Comput Phys 227:3921–3939
11. Sanapala VS, Rajkumar M, Velusamy K, Patnaik BSV (2018) Numerical simulation of parametric liquid sloshing in a horizontally baffled rectangular container. J Fluids Struct 76:229–250
12. Li Q, Ma X, Wang T (2011) Equivalent mechanical model for liquid sloshing during draining. Acta Astronaut 68:91–100
13. Yang C, Niu Y, Zhang R (2021) Numerical analyses of liquid slosh by Finite volume and Lattice Boltzmann methods. Aerosp Sci Technol 113:106681
14. Liu Z, Chen H, Chen Q, Chen L (2021) Numerical study on thermodynamic performance in a cryogenic fuel storage tank under external sloshing excitation. Int J Aeronaut Space Sci 22:1062–1074
15. Ibrahim RA, Pilipchuk VN, Ikeda T (2001) Recent advances in liquid sloshing dynamics. Appl Mech Rev 54:133–199
16. Yue B, Zhu L (2014) Hybrid control of liquid-filled spacecraft maneuvers by dynamics inversion and input shaping. AIAA J 52:618–626
17. Wang T, Miao N, Li J (2016) Large-amplitude sloshing analysis and equivalent mechanical modeling in spherical tanks of spacecraft. J Spacecr Rockets 53:500–506
18. Chung B, Kim T, Suh J, Han J, Lee J, Jung H (2020) Vibration analysis of SAR antenna reflector during satellite maneuver considering the propellant sloshing effect. Trans Korean Soc Noise Vib Eng 30:52–59
19. Vreeburg JPB (1997) Dynamics and control of a spacecraft with a moving pulsating ball in a spherical cavity. Acta Astronaut 40:257–274
20. Lee D, Cho M, Choi H, Tahk M (2019) Pendulum modeling of sloshing motion using particle swarm optimization. Int J Aeronaut Space Sci 20:172–182
21. Godderidge B, Turnock SR, Tan M (2012) A rapid method for the simulation of sloshing using a mathematical model based on the pendulum equation. Comput Fluids 57:163–171
22. Kana DD (1989) Validated spherical pendulum model for rotary liquid slosh. J Spacecraft 26:188–195
23. Cui D, Yan S, Guo X, Gao RX (2014) Parametric resonance of liquid sloshing in partially filled spacecraft tanks during the powered-flight phase of racket. Aerosp Sci Technol 35:93–105
24. Constantin L, De Courcy J, Titurus B, Rendall TCS, Cooper JE (2021) Analysis of damping from vertical sloshing in a SDOF system. Mech Syst Signal Proc 152:107452
25. Shi Z, Xiao H, Zhu Q, Wang Q (2020) Resonant frequencies analysis and vibration control of fluid in three-dimensional (3D) moonpool: Analytical modeling and experimental study. Mech Syst Signal Proc 144:106882
26. Shadloo MS, Oger G, Touze DL (2016) Smoothed particle hydrodynamics method for fluid flows, towards industrial applications: motivations, current state, and challenges. Comput Fluids 136:11–34
27. Ye T, Pan D, Huang C, Liu M (2019) Smoothed particle hydrodynamics (SPH) for complex fluid flows: Recent developments in methodology and applications. Phys Fluids 31:011301
28. Liu M, Liu G (2010) Smoothed particle hydrodynamics (SPH): an overview and recent developments. Arch Comput Methods Eng 17:25–76
29. Violeau D, Rogers BD (2016) Smoothed particle hydrodynamics (SPH) for free-surface flows: past, present and future. J Hydraul Res 54:1–26
30. L. Han, X. Hu, SPH modeling of fluid-structure interaction, in: SPHERIC Beijing, October (2017).
31. Xu R, Stansby P, Laurence D (2009) Accuracy and stability in incompressible SPH (ISPH) based on the projection method and a new approach. J Comput Phys 228:6703–6725
32. Shao S, Lo EYM (2003) Incompressible SPH method for simulating Newtonian and non-Newtonian flows with a free surface. Adv Water Resour 26:787–800
33. Ihmsen M, Cornelis J, Solenthaler B, Horvath C, Teschner M (2014) Implicit Incompressible SPH. IEEE Trans Vis Comput Graph 20:426–435
34. Cao X, Tao L, Zhang A, Ming F (2019) Smoothed particle hydrodynamics (SPH) for coupled analysis of a damaged ship with internal sloshing in beam seas. Phys Fluids 31:032103
35. Marsh AP, Prakash M, Semercigil SE, Turan OF (2010) A shallow-depth sloshing absorber for structural control. J Fluids Struct 26:780–792
36. Lee ES, Moulinec C, Xu R, Violeau D, Laurence D, Stansby P (2008) Comparisons of weakly compressible and truly incompressible algorithms for the SPH mesh free particle method. J Compu Phys 227:8417–8436
37. Ren Y, Khayyer A, Luo M, Lin P (021) Comparative analysis of standard-WCSPH, δ-SPH and Riemann-SPH in modeling free-surface flows. In: Proceedings of the 31th International Ocean and Polar Engineering Conference
38. Sun P, Colagrossi A, Zhang A (2018) Numerical simulation of the self-propulsive motion of a fishlike swimming foil using the δ^+-SPH model. Theor Appl Mech Lett 8:115–125
39. Zhang C, Hu X, Adams NA (2017) A weakly compressible SPH method based on a low-dissipation Riemann solver. J Comput Phys 335:605–620
40. Zhang C, Rezavand M, Hu X (2020) Dual-criteria time stepping for weakly compressible smoothed particle hydrodynamics. J Comput Phys 404:109135

41. Hu W, Guo G, Hu X, Negrut D, Xu Z, Pan W (2019) A consistent spatially adaptive smoothed particle hydrodynamics method for fluid-structure interaction. Comput Methods Appl Mech Engrg 347:402–424
42. Rakhsha M, Yang L, Hu W, Negrut D (2021) On the use of multibody dynamics techniques to simulate fluid dynamics and fluid-solid interaction problems. Multibody Syst Dyn 53:29–57
43. Yu Q, Wang T, Li Z (2019) Rapid simulation of 3D liquid sloshing in the lunar soft-landing spacecraft. AIAA J 57:4504–4513
44. Li J, Cao D, Pan K (2020) Dry-friction-induced self-excitation of a rectangular liquid-filled tank. Nonlinear Dyn 102:1337–1359
45. Li J, Cao D, Pan K (2022) Hydrodynamics with complex boundary motions by non-inertial SPH method and its application in attitude-liquid-control coupled dynamics of a liquid-filled quadrotor UAV. Mech Syst Signal Proc 163:108066
46. Li J, Wang F, Cao M et al (2024) Attitude motion and nonlinear free-surface deformation of stone-skipping over shallow water. Phys Fluids 36:126105
47. Zuo Z (2010) Trajectory tracking control design with command-filtered compensation for a quadrotor. IET Contr Theory Appl 4:2343–2355
48. Zhuang H, Sun Q, Chen Z, Zeng X (2021) Robust adaptive sliding mode attitude control for aircraft systems based on back-stepping method. Aerosp Sci Technol 118:107069
49. Yu J, Shi P, Dong W, Yu H (2015) Observer and command-filter-based adaptive fuzzy output feedback control of uncertain nonlinear systems. IEEE Trans Ind Electron 62:5962–5970
50. Sun K, Tang J, Wu Z, Li Y, Cao D (2024) Coupled nonlinear vibration characteristics of quasi-zero-stiffness Gough-Stewart isolation platform. Aerosp Sci Technol 152:109352
51. J. Jiang, J. Tang, K. Sun, H. Chen, Y. Li, D. Cao, Data-driven model identification and control of the quasi-zero-stiffness system, Nonlinear Dyn. Online. doi.org/https://doi.org/10.1007/s11071-024-09811-5
52. K. Sun, J. Tang, Y. Yang, B. Jiang, Y. Li, D. Cao, Active Control of Quasi-Zero-Stiffness Vibration Isolator with Variable Load, Int. J. Struct. Stab. Dy. Online. doi.org/https://doi.org/10.1142/S0219455424502432
53. Wang X, Wang G, Chen Z, Lim CW, Li S, Li C (2024) Controllable flexural wave in laminated metabeam with embedded multiple resonators. J Sound Vib 581:118386
54. Li HN, Wang W, Lai SK, Yao LQ, Li C (2024) Nonlinear vibration and stability analysis of rotating functionally graded piezoelectric nanobeams. Int J Struct Stab Dyn 24:2450103
55. Li HN, Yao LQ, Li C, Guo LM (2024) Capturing the nonlocal effect using a novel hybrid 8-node plate element based on the Hellinger-Reissner variational principle, Engineering with Computers. Online. https://doi.org/10.1007/s00366-024-02061-4
56. Guo LM, Cai JW, Xie ZY, Li C (2024) Mechanical responses of symmetric straight and curved composite microbeams. Journal of Vibration Engineering & Technologies 12:1537–1549
57. Xie ZY, Guo LM, Li C, Shi YT, Han B (2024) Modeling the deformation of thin-walled circular tubes filled with metallic foam under two lateral loading patterns. Structures 69:107289
58. Pandey DK, Sharma MK, Mishra SK (2019) A compliant tuned liquid damper for controlling seismic vibration of short period structures. Mech Syst Signal Proc 132:405–428
59. Altunisik AC, Yetisken A, Kahya V (2018) Experimental study on control performance of tuned liquid column dampers considering different excitation directions. Mech Syst Signal Proc 102:59–71